BNL-203531-2018-JAAM

2D molybdenum and vanadium nitrides synthesized by ammoniation of 2D transition metal carbides (MXenes)

P. Urbankowski, L. Zhang

To be published in "Nanoscale"

November 2017

Center for Functional Nanomaterials

Brookhaven National Laboratory

U.S. Department of Energy

USDOE Office of Science (SC), Basic Energy Sciences (BES) (SC-22)

DISCLAIMER

2D molybdenum and vanadium nitrides synthesized by ammoniation of 2D transition metal carbides (MXenes)

Patrick Urbankowski,[1] Babak Anasori,[1] Kanit Hantanasirisakul,[1] Long Yang,[2] Lihua Zhang,[3] Bernard Haines,[1] Steven J. May,[1] Simon J. L. Billinge,[2,4] Yury Gogotsi[1†]

[1]A.J. Drexel Nanomaterials Institute and Department of Materials Science & Engineering, Drexel University, Philadelphia, PA 19104, USA
[2]Department of Applied Physics and Applied Mathematics, Columbia University, New York, NY 10027, USA
[3]Center for Functional Nanomaterials, Brookhaven National Laboratory, Upton, NY 11973, USA
[4]Condensed Matter Physics and Materials Science Department, Brookhaven National Laboratory, Upton, NY 11973, USA

[†]Correspsonding author:
Y. Gogotsi (gogotsi@drexel.edu) Tel.: +1-215-895-6446 Fax: +1-215-895-1934

Abstract

MXenes are a rapidly growing class of 2D transition metal carbides and nitrides, finding applications in fields ranging from energy storage to electromagnetic interference shielding and transparent conductive coatings. However, while more than 20 carbide MXenes have already been synthesized, Ti_4N_3 and Ti_2N are the only nitride MXenes reported so far. Here by ammoniation of Mo_2CT_x and V_2CT_x MXenes at 600 ºC, we report on their transformation to 2D metal nitrides. Carbon atoms in the precursor MXenes are replaced with N atoms, resulting from the decomposition of ammonia molecules. The crystal structures of the resulting Mo_2N and V_2N were determined with high-resolution transmission electron microscopy and X-ray pair distribution function analysis. Our results indicate that Mo_2N retains the MXene structure and V_2N transforms to a mixed layered structure of trigonal V_2N and cubic VN. Temperature-dependent resistivity measurements of the nitrides reveal that they exhibit metallic conductivity, as opposed to semiconductor-like behavior of their parent carbides. As importantly, room-temperature conductivity values of Mo_2N and V_2N are three and one order of magnitude larger than those of the Mo_2CT_x and V_2CT_x precursors, respectively. This study shows how gas treatment synthesis such as ammoniation can transform carbide MXenes into 2D nitrides with higher electrical conductivities and metallic behavior, opening a new avenue in 2D materials synthesis.

Introduction

MXenes, a family of two-dimensional (2D) transition metal carbides, carbonitrides and nitrides, have attracted much attention for their excellent properties and applications, and research is continuing to grow.[1-5] These properties, including their hydrophilic surfaces and high electrical conductivities,[1, 6, 7] make them promising in energy storage devices,[6-9] electromagnetic interference (EMI) shielding,[10, 11] and many other applications.[12-21] Carbide MXenes have been most commonly produced by selectively etching out the A-element layer from a MXene's corresponding ternary carbide precursor (usually a MAX phase) in hydrofluoric acid (HF).[1] The term MAX phase is derived from its constituent elements in the general formula $M_{n+1}AX_n$, where M is an early transition metal, A is a group IIIA or IVA element, X is C and/or N, and n = 1, 2 or 3.[2] For example, when Ti_3AlC_2 is treated in HF, Al is selectively etched and this process yields the MXene $Ti_3C_2T_x$, where T_x represents the terminating groups along the two faces of each 2D flake such as –F, –O, and –OH.[2]

Nitride MXenes have attracted attention for their potential applications in energy storage and plasmonics[22, 23] due to their higher electrical conductivities,[24] which are expected to be higher than those of carbide MXenes.[25] For example, 2D MoN films have been shown to exhibit a very high volumetric capacitance of 928 F cm^{-3} in sulfuric acid electrolyte and excellent rate performance.[26] MXenes theoretically include the same number of nitrides and carbides.[27] Since attempts to synthesize nitride MXene via methods used for carbide MXenes have failed, however, it was not until recently when the first nitride MXene (titanium nitride, Ti_4N_3) was synthesized with a novel molten salt etching synthesis approach,[28, 29] followed by the synthesis of Ti_2N.[23] Lack of focus on finding high-yield synthesis methods have prevented not only MXene nitrides, but 2D nitrides in general, and their applications from developing further. Only a few

2D nitrides including MoN,[26] GaN,[30] Ti_4N_3,[28] and Ti_2N [23] have been reported so far. Current strategies for synthesis of 2D nitrides are mostly limited to exfoliation of layered materials, while a gas-phase synthesis of GaN monolayers under graphene also exists.[30] Several of those studies, however, lacked focus on upscaling the methods and yielding 2D metal nitrides which could be easily be implemented into devices, which is a major focus of this study.

Exfoliation of nitride MAX phases in aqueous hydrofluoric acid solutions, a common approach in synthesizing carbide MXenes, has not been successful. The instability of nitride MXenes in aqueous hydrofluoric acid, contrary to carbide MXenes, is related to how the formation energies of nitride MXenes (for example, $Ti_{n+1}N_n$) from their MAX phases (for example, $Ti_{n+1}AlN_n$) are greater than those of carbide MXenes ($Ti_{n+1}C_n$) from their MAX phase precursors ($Ti_{n+1}AlC_n$).[31] It is also related to how cohesive energies of nitride MXenes are less than those of corresponding carbide MXenes.[31] In other words, preparing nitride MXenes via etching in aqueous hydrofluoric acid has not been successful because it has not been possible to selectively etch the Al layer in the MAX phase precursor (e.g. Ti_4AlN_3) without dissolving the product.[28] While high-temperature chemical exfoliation methods for producing nitrides exist, high-yield gas-phase synthesis methods for producing 2D nitrides have not been focused on.

Heat treatment in ammonia (ammoniation) has been used on metal oxides to either N-dope them or transform oxides to 3D nitrides. Although ammoniation of 2D precursors such as GaSe to yield the 2D metal nitride GaN has been reported, the extent of the route of synthesizing other potential 2D metal nitrides via ammoniation has not been fully realized.[32] TiO_2 can be N-doped by nitridation at 600 ºC,[33, 34] and recently reported nitridation attempts of Ti_3C_2 have yielded only N-doped 2D carbides.[35] Ti_3C_2 was doped with nitrogen atoms by ammoniation at temperatures up to 700 °C in which N comprised up to 20.7 at.% of the product.[35] It was only

recently when synthesis of 2D metal nitrides via ammoniation was reported, including 2D MoN via the ammoniation of MoO_3-coated NaCl.[36] In this study, we report the first transformation of Mo_2CT_x and V_2CT_x carbide MXenes into 2D metal nitrides via ammoniation at 600 °C. It is important to note that unlike previously reported 2D MoN and V_2N via salt-templated synthesis with 2D metal oxide precursors,[37] the 2D metal nitrides reported here, synthesized with carbide MXene precursors, have different crystal structures than those previously reported. Our results indicate that Mo_2N retains the MXene structure and V_2N transforms to a mixed layered structure of trigonal V_2N and cubic VN.

Experimental

Synthesis

The Mo_2CT_x and V_2CT_x MXenes were discovered recently and several works have since been reported on their properties and novel synthesis methods.[8, 38-41] Experimental research on thermoelectric properties of Mo_2C has been studied.[42] 2D carbide MXenes, produced after etching their precursor MAX phase, typically have multilayered structures.[2] Other bulk precursors for MXenes also exist.[43, 44] Multilayered powders can be delaminated into single- and few-layer flakes in solution using solvents and sonication, which can be filtered to form flexible, freestanding films.[2] Films of delaminated Mo_2CT_x and V_2CT_x flakes with thicknesses ranging from 2 to 20 μm are described in the Supporting Information. To synthesize nitride MXenes, multilayer powders and delaminated films of Mo_2CT_x and V_2CT_x were treated at 600 °C for 1 h at a heating rate of 10 °C/h in an ammonia, NH_3, atmosphere and cooled at the same rate. The ammonia flow rate through the reactor was approximately 300 cm^3/min. During the reaction, nitridation occurs by the replacement of C atoms, in the Mo_2CT_x and V_2CT_x, with N atoms. A

schematic of the process is shown in **Scheme 1**. The synthesis process is described in complete detail in the Supporting Information.

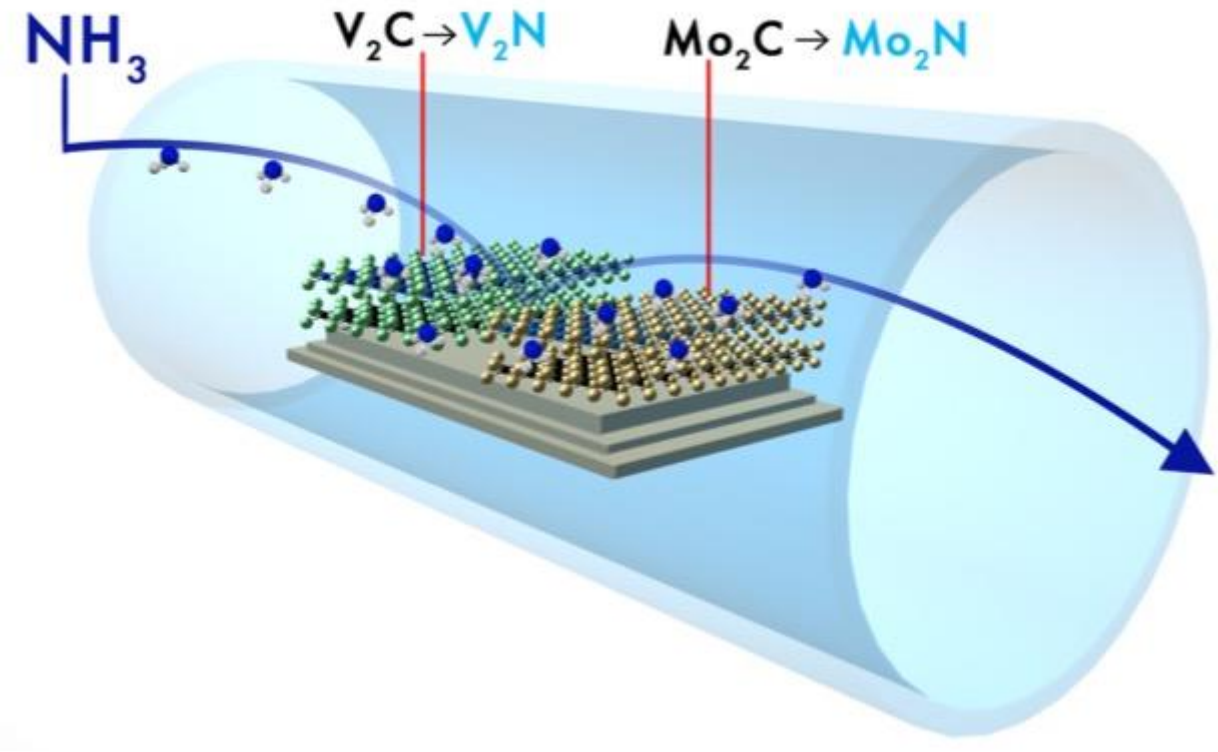

Scheme 1. Synthesis of 2D transition metal nitrides can be achieved by ammoniation of MXenes (Mo_2CT_x and V_2CT_x) at elevated temperatures.

Results

Characterization

To determine whether nitridation occurred, as the first step, energy dispersive X-ray spectroscopy (EDX) in a scanning electron microscope (SEM) was performed to analyze the qualitative atomic compositions of the ammoniated products. SEM images of the delaminated MXene films after annealing in ammonia at 600 °C for 1 h are shown in Fig. 1a and b, for Mo_2N and V_2N, respectively. The structures of both samples suggest that the layered structure remains after ammoniation. Table 1 shows the atomic composition ratios detected by EDX, normalized to

the metal M (Mo or V) = 2.00. As shown in Table 1, for Mo_2CT_x before treatment, the Mo : N : C ratio is 2.00 : 0.00 : 5.35, and after ammoniation at 600 °C, the nitrogen replacing carbon is evident by the change in ratio to 2.00 : 2.04 : 0.00. For V_2CT_x before treatment, the V : N : C ratio is 2.00 : 0.00 : 3.91, which changes to 2.00 : 2.46 : 0.58 after ammoniation at 600 °C. To optimize the ammoniation conditions, several temperatures were attempted. As evident in Table 1, as the temperature of ammoniation increases from 400 °C to 600 °C, the ratio of N to C greatly increases, with the amount of C decreasing most significantly at the 600 °C treatment. Since EDX does not quantify light elements (C and N) accurately, these results are presented to show not exact compositions of the products, but rather the trend of the composition of nitrogen and carbon in the products as the temperature is varied. Low- and high-magnification SEM images shown in Fig. S1 in the Supporting Information confirm that no separate oxide particles are present. Oxidation and the formation of oxides can occur when annealing MXenes in high temperature,[2] but the absence of oxide particles confirms that the material is stable against oxidation in ammonia, up to at least 600 °C.

Table 1. Summary of elemental analysis in EDX before and after ammoniation at various temperatures for 1 h, listed with standard error of the mean. Atomic ratios are normalized to Mo or V = 2.00 ± 0.00.

	Mo	N	C	O	F
Mo_2C before	2.00 ± 0.00	–	5.35 ± 1.46	2.87 ± 0.18	0.32 ± 0.05
NH_3 600 °C	2.00 ± 0.00	2.04 ± 0.05	–	1.02 ± 0.05	–
NH_3 500 °C	2.00 ± 0.00	1.76 ± 0.18	3.03 ± 0.03	2.16 ± 0.08	–
NH_3 400 °C	2.00 ± 0.00	1.55 ± 0.22	2.13 ± 0.18	1.89 ± 0.13	–

	V	N	C	O	F
V_2C before	2.00 ± 0.00	–	3.91 ± 0.10	1.40 ± 0.01	1.30 ± 0.05
NH_3 600 °C	2.00 ± 0.00	2.46 ± 0.08	0.58 ± 0.02	–	–
NH_3 500 °C	2.00 ± 0.00	1.34 ± 0.27	1.19 ± 0.04	0.30 ± 0.10	0.16 ± 0.03
NH_3 400 °C	2.00 ± 0.00	0.86 ± 0.06	1.80 ± 0.06	1.43 ± 0.07	0.67 ± 0.02

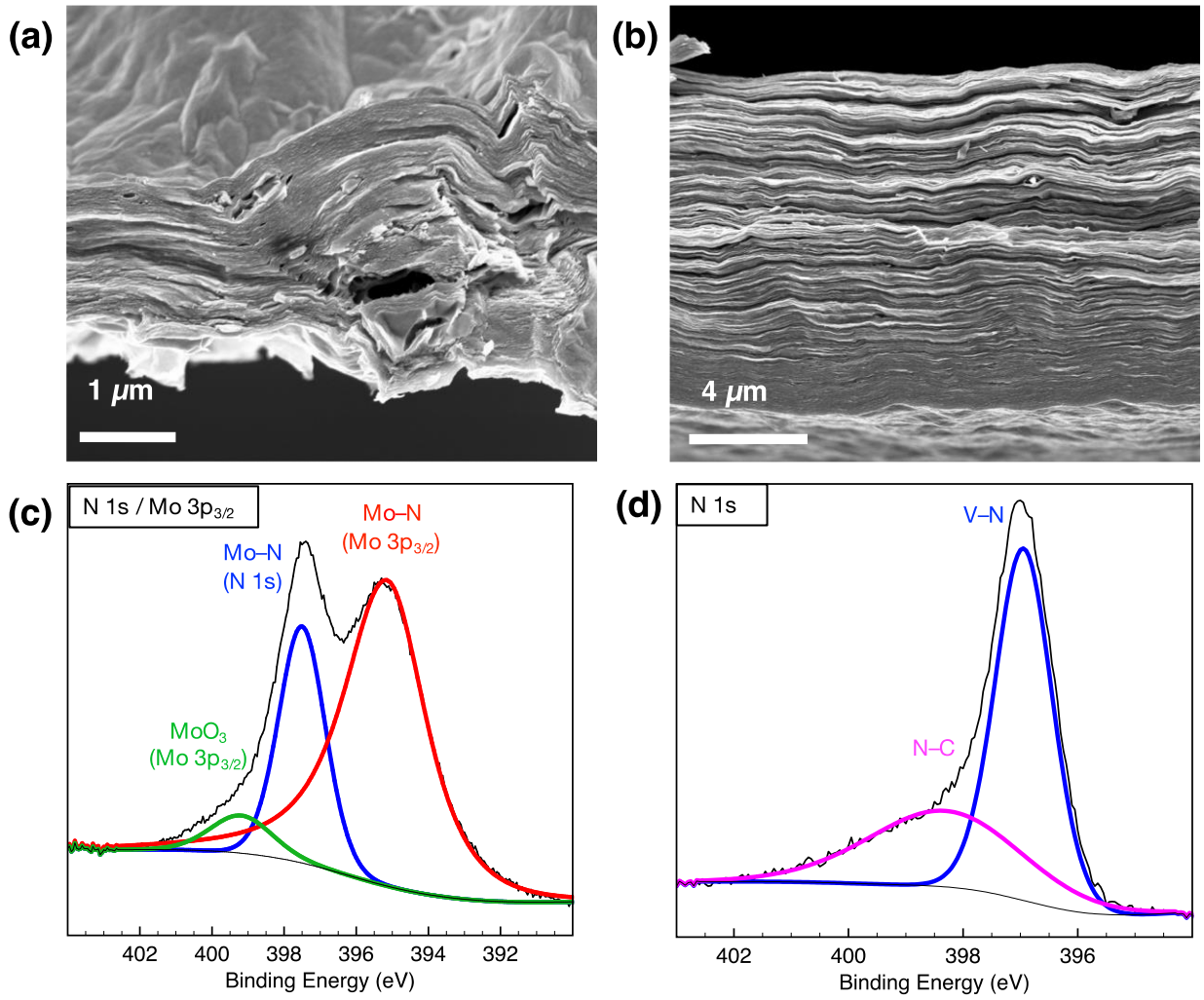

Fig. 1. The layered, 2D morphology of the delaminated film is shown in the SEM images in (a) Mo_2N and (b) V_2N. Evidence for Mo–N bonding in Mo_2N is shown in the XPS spectrum in the N 1s / Mo $3p_{3/2}$ region in (c), while evidence of V–N bonding in V_2N is shown in (d).

To understand the nature of N detected in EDX and to confirm that nitridation occurred, X-ray photoelectron spectroscopy (XPS) measurements were performed on the Mo_2N and V_2N films. XPS was performed to confirm that N was bonded to the metal atoms (Mo or V), and that the C-metal bonding was eliminated or diminished. High-resolution XPS spectra deconvolution for the N 1s region is shown for Mo_2N (Fig. 1c) and V_2N (Fig. 1d). Additional deconvolution for other regions are shown in Fig. S2 in the Supporting Information. The deconvolution for the

various species and the elemental compositions extracted from the high-resolution spectra are tabulated in Tables S1 and S2 in the Supporting Information for Mo_2N and V_2N, respectively.

For Mo_2N, Fig. 1c shows the high-resolution spectrum of the N 1s / Mo $3p_{3/2}$ region. This region contains components from two different orbitals that are N 1s and Mo $3p_{3/2}$. This region was fitted by components corresponding to the following species: Mo–N (Mo $3p_{3/2}$), Mo–N (N 1s) and MoO_3 (Mo $3p_{3/2}$), confirming that N is bonded to Mo. Moreover, as indicated in Table S1 and Table S2 in the Supporting Information, the C 1s regions of both nitrides show that there is either no or a very insignificant metal–carbon component for V_2N and Mo_2N, respectively , which should typically appear at ~282 eV,[45] confirming that N replaced C in these systems. The composition of all components fitted for this Mo_2N sample are tabulated in Table S1. The fractions of N–Mo–T_x (Mo 3d) (21 at.%), Mo–N (Mo $3p_{3/2}$) (21 at.%) and Mo–N (N 1s) (22 at.%) are among the most prominent components. By taking the ratios of these two Mo components and one N component, the fraction of 2 : 1 ratio of Mo : N suggests a formula of Mo_2NT_x. This is, however, difficult to quantify, because a miniscule amount of the N–Mo–T_x (Mo 3d) component may also be attributed to C–Mo–T_x bonding. A C-Mo-T_x component was assigned in the C 1s spectrum (Fig. S2c), indicating some non-nitridized carbide MXene particles are present (less than 1.0 % of the area all fitted components in all regions, as shown in Table S1). The T_x indicates the oxygen and hydroxyl terminating functional groups that are likely present on the surface, as suggested by the species detected in the O 1s region shown in Fig. S2b.

For V_2N, Fig. 1d shows the high-resolution spectrum of the N 1s region. This region was fitted by components corresponding to the species V–N and N–C. These two regions confirm that N is bonded to V in this system. The composition of all components fitted for this sample

are tabulated in Table S2. Based on these fractions of components in the V 2p and N 1s regions, if one assumes that all components in the V 2p region are a part of the nitride product, and the higher valency V^{4+} and V^{5+} components are oxygen-terminated –V–N–O_x components, then the 2 : 1 ratio of V : N may suggest a chemical formula of V_2NT_x. Similar to Mo_2CT_x, the T_x in this formula indicates the oxygen surface groups on the surface that were detected, shown in Fig. S2e. Based on XPS, we can conclude that the C that was detected in EDX is not in the V_2N structure but rather from adventitious carbon.[46]

After confirming that these products were nitrides, X-ray diffraction (XRD) was carried out on the ammoniated samples to determine whether the MXene structure was kept or new crystal phases were formed. As shown in the XRD patterns in Fig. 2a, after the ammoniation of Mo_2CT_x, the expected layered structure of a MXene is still maintained as evidenced by the (002) peak in the top pattern for Mo_2N, which represents the distance between MXene layers.[2] The (002) basal plane peak for Mo_2CT_x MXenes exists typically in the range of 2θ = 3 to 11°, depending on the number of intercalated water and other molecules.[45,47] The (002) peak measured from Mo_2CT_x appears at about 7°, due to the expansion of the layers after the intercalation of water and the delaminating solvent tetrabutylammonium hydroxide (TBAOH), as described in the Supporting Information.[45] After ammoniation at 600 °C, the (002) peak shifts to ~11.4°, corresponding to an average interlayer distance of 7.8 Å. This value is in the range of what is predicted for the functionalized M_2XT_x MXenes with no intercalated molecules (M represents a transition metal).[47] As shown in Fig. S3a in the Supporting Information, the Mo_2XT_x (X referring to either C or N) MXene (002) peak shifts to about 2θ = 9° after the sample was ammoniated at 400 °C and 500 °C. It is only after the sample was ammoniated at 600 °C that the peak shifts to about 11°, indicating that the spacing between the 2D layers is smaller after the

higher temperature processing. We attribute this contraction to the complete removal of intercalated molecules and possibly some of the functional groups such as –F and of confined water.[47] There are other peaks at larger 2θ observed for the as-synthesized and ammoniated at 600ºC Mo_2CT_x that all correspond to the (*00l*) basal plane peaks, indicating that the layer stacking is somewhat regular. In the case of ammoniation at 600ºC, two peaks are located at ~23 and 34º corresponding to the (004) and (006) peaks of MXene. This suggests that the resulting phase is Mo_2NT_x, as these peaks correspond to higher-order ordering of MXene layers. The other possible phase to form is hexagonal MoN (*h*-MoN). However, *h*-MoN XRD peaks do not match any peaks of the collected pattern. The first and major peak of *h*-MoN at 36º corresponds to its (200) planes,[36] where there is no peak observed in the Mo_2NT_x pattern (Fig. 2a).

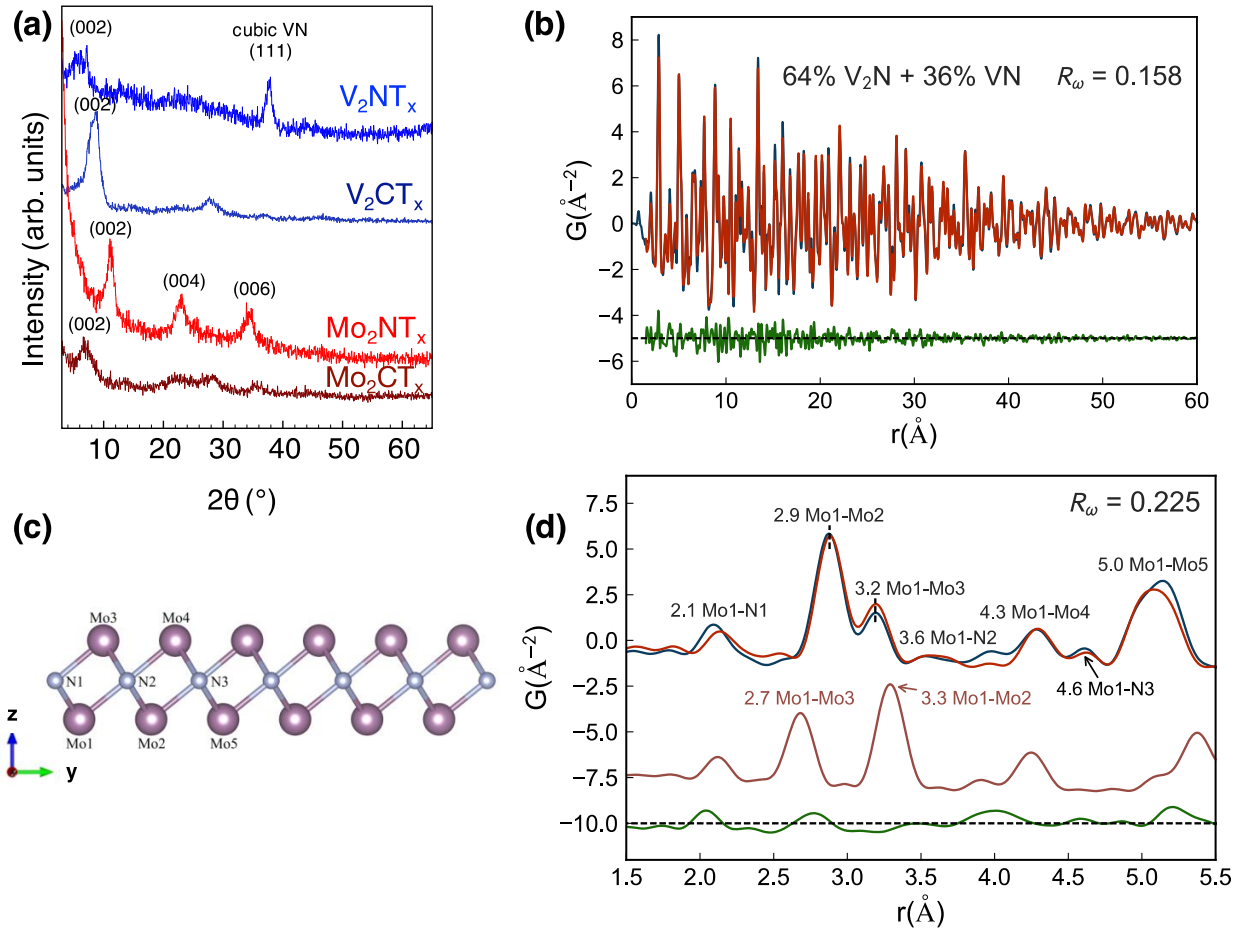

Fig. 2. (a) XRD patterns of Mo_2CT_x and V_2CT_x before and after (Mo_2NT_x and V_2NT_x) ammoniation at 600 °C for 1 h. After Mo_2CT_x was annealed at 600 °C it formed Mo_2NT_x and maintained its 2D MXene structure as evidenced by the presence of the (002) peak at $2\theta = 11°$. For V_2NT_x (top blue curve), a broad peak appears at $2\theta = 7.0°$, while the presence of a non-MXene nitride is evidenced by the peak at 37°. (b) X-ray pair distribution function (PDF) fit (red curve) of the 64% V_2N + 36% VN (mass ratio) mixed phase model to the measured data (blue) with difference curve offset below (green). R_ω is the goodness of fit (a lower value corresponds to better fit). (c) Single slab model of Mo_2N MXene (space group $P6_3/mmc$) after structure refinement, projected along the [100] direction. (d) PDF fit (top red curve) of the Mo_2N single slab model after structure refinement to the measured data (top blue) with a difference curve offset (bottom green). Simulated PDF of the initial Mo_2N MXene single slab model (having the same atomic positions as the precursor Mo_2C MXene structural model) without structure refinement (middle brown) is shown in the offset below the measured data (top blue).

The (002) peak of V_2CT_x consists of a doublet in the range of about $2\theta = 8\text{-}9°$, indicating intercalated water and TBAOH molecules and functional groups. There are higher order (*00l*) peaks at lower intensities, indicating the regular periodic stacking of MXene layers over an extended range. After ammoniation, a broad peak appears around 7.0°, which can be related to the (002) peak of a MXene structure, and perhaps indicating that the interlayer spacing is increased after ammoniation. Additionally, ammoniation results in the appearance of a new peak at 37°, which can be assigned to the (111) peak of cubic VN.[48, 49]

To obtain a more quantitative determination of the atomic structure and morphology of the nitride flakes, X-ray pair distribution function (PDF) analysis was conducted on the Mo_2NT_x and V_2NT_x.[50, 51] The samples analyzed were prepared by ammoniating multilayered Mo_2CT_x and V_2CT_x, respectively. The data acquisition, data reduction, and structural modeling are described in greater detail in the Supporting Information.[52-57]

We first discuss the structure of the Vanadium compound. The measured PDF data have sharp peaks over a wide range of *r* (blue curve in Fig. 2b) indicating that the nitride products have relatively well-ordered structures and are of sufficient quality to refine quantitative structures. The data in the high-*r* region (up to $r = 60$ Å) were well fit to a trigonal V_2N structure

(space group *P*-31*m*) (Fig. S4) with atoms sitting at the following special positions: V (*x*, 0, *z*), N1 (1/3, 2/3, 1/2), and N2 (0, 0, 0).[58] The fit appears quite good in the high-*r* region however, especially in the low-*r* region, there is significant signal in the difference curve (green curve offset below in in Figs. S5a and S5b) suggesting that this model does not explain all the features observed in the data. We therefore added a second phase, cubic VN (space group *Fm*-3*m*) (Fig. S6) with a finite particle size, to the modeling with atoms sitting at the following special positions: V (0, 0, 0) and N (1/2, 1/2, 1/2).[59] The improvement in the fit is good with a refined mass fraction of 36% and a VN phase with particle size of around 2 nm. The PDF fit of this mixed phase model is shown in Fig. 2b and the refined structural parameters are shown in Table 2.

Table 2. Structure refinement result of the Vanadium product, fit to trigonal V_2N and cubic VN mixed phase model. Q_{damp} and Q_{broad} parameters were refined in a fit to a standard calibration sample (see SI for details) and then fixed to 0.0369 $Å^{-1}$ and 0.0131 $Å^{-1}$, respectively. For the VN phase, its lattice parameters were constrained as $a = c$ due to cubic symmetry, and its isotropic atomic displacement parameters U_{iso}(V) and U_{iso}(N) were constrained in the same way as those in the V_2N phase. Spdiameter is the particle diameter parameter for PDF shape damping function.

Fitting Range (Å)	1.5 to 60	
R_ω	0.158	
Phase	V_2N	VN
Mass Ratio	64%	36%
a (Å)	5.0415	4.1267
c (Å)	4.3724	4.1267
x (V)	0.6716	-
z (V)	0.7509	-
U_{iso}(V) ($Å^2$)	0.0032	0.0032
U_{iso}(N) ($Å^2$)	0.0118	0.0118
Spdiameter (Å)	-	21.3486

The structure of Mo_2N, on the other hand, can be described as a distorted MXene ($P6_3/mmc$) structure, created by cutting a single slab of atoms from its respective crystal

structure, shown in Fig. 2c.[60] We used the Debye scattering equation to calculate the PDF of a single slab using the DiffPy-CMI program.[57, 61] It is clear from the PDF of Mo_2N in Fig. 2d (blue curve), that the local structure has lower symmetry than the V_2N, for example the PDF peak centered around r = 3 Å, which is the Mo-Mo nearest neighbor peak, is split into two. Such a distinct set of Mo-Mo distances was seen in the hexagonal ($P6_3/mmc$) carbide Mo_2C MXene precursor structure. However, the simulated PDF of the Mo_2C structural model (brown curve in Fig. 2d) did not fit the measured data (blue curve in Fig. 2d) well. We were able to fit the measured data well over the low-r range by staying in the same space group, but by squeezing a single slab of Mo_2N along in-plane dimensions and extending along the out-of-plane dimension (z-direction). This caused the distance between nearest Mo atoms on the same z-coordinate plane (e.g. Mo1-Mo2 in Fig. 2c) to decrease from 3.3 to 2.9 Å, while the distance between nearest Mo atoms separated along the z-direction (but still within a single slab, e.g. Mo1-Mo3 in Fig. 2c) to increase from 2.7 to 3.2 Å. The distortion in the Mo_2N structure is the opposite from that in the Mo_2C. In the latter, out-of-plane Mo-Mo distances are shorter than the in-plane Mo-Mo distances. This has implications for the electronic structure and electrical properties that require further study. The refined structural parameters are shown in Table 3.

Table 3. The structure refinement result of Mo_2N. The Mo_2N (space group is $P6_3/mmc$) single slab model is created by cutting a single slab of atoms from its respective bulk crystal structure. The atoms are on the following special positions: Mo1 at (1/3, 2/3, z), Mo2 at (0, 0, z), and N (1/3, 2/3, z). Q_{damp} and Q_{broad} parameters were refined in a fit to a standard calibration sample (see SI for details) and then fixed to 0.0369 $Å^{-1}$ and 0.0131 $Å^{-1}$, respectively.

Fitting Range (Å)	1.5 to 5.5
R_ω	0.225
a (Å)	2.8850
z (Mo1)	0.4348
z (Mo2)	0.0713
z (N)	0.0019
U_{iso} (Mo) ($Å^2$)	0.0048
U_{iso} (N) ($Å^2$)	0.0021

To corroborate conclusions based on the X-ray PDF, high-resolution transmission electron microscopy (TEM) was then used. TEM images were acquired on a JEOL2100F high resolution TEM, at accelerating voltage 200 kV. For the TEM images and selected area electron diffraction (SAED) patterns in Fig. 3, as-produced multilayered Mo_2NT_x and V_2NT_x (ammoniated Mo_2CT_x and V_2CT_x at 600 ºC) were examined instead of delaminated films to minimize the effects of post-treatment. Because these are multilayered powders, they are relatively thicker than would be delaminated single-layer sheets of Mo_2NT_x and V_2NT_x. As shown in the inset in Fig. 3a, the SAED for the Mo_2NT_x particle is hexagonal, similar to the pattern of its carbide MXene precursor's basal plane (space group $P6_3/mmc$). The distance between the nearest spots in SAED is 4.16 nm^{-1}. It does not, therefore, correspond to the distance expected for 2D h-MoN for the (001) plane's pattern (5.18 nm^{-1}),[36] but rather to a distorted $P6_3/mmc$ structure, which is in agreement with the XRD and X-ray PDF results. For the V_2NT_x SAED in Fig. 3b, the hexagonal pattern shown could be attributed to the (001) plane of trigonal V_2N or the (111) plane of the cubic VN present in the sample, as determined by the X-ray PDF and XRD results.

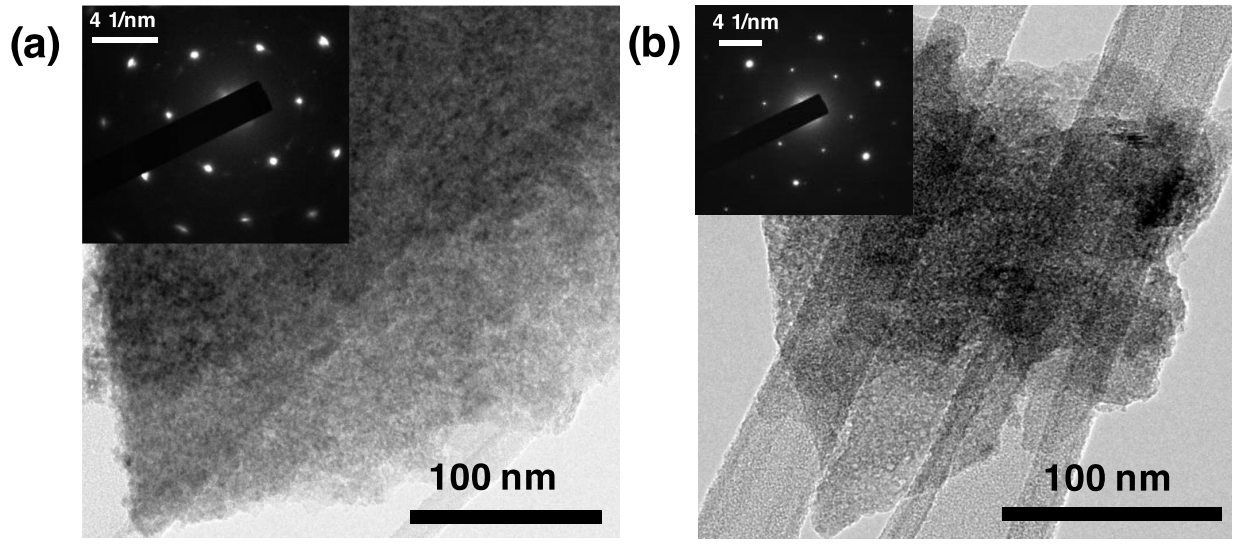

Fig. 3. (a) TEM micrograph of Mo_2NT_x synthesized by the ammoniation of multilayered Mo_2CT_x at 600 °C. (b) TEM micrograph of V_2NT_x synthesized by the ammoniation of multilayered V_2CT_x at 600 °C. The insets show the selected-area diffraction patterns these regions. Each shows hexagonal basal plane symmetry. In the case of (a), this could be attributed to the (001) plane of the MXene structure. In the case of (b), this could be attributed to the (001) plane of trigonal V_2N, or (111) plane of the cubic VN impurity.

Electrical Conductivity Characterization

After confirming the crystal structure and composition of these two transition metal nitrides Mo_2NT_x and V_2NT_x, electronic properties were measured. Electronic properties of Mo_2CT_x and V_2CT_x before and after heat treatments were studied in a Quantum Design EverCool II Physical Property Measurement System (PPMS). A free-standing film with a thickness ~ 20 μm of each sample was cut to a 5×5 mm square, and silver wires were attached onto the film in a 4-point probe geometry using adhesive silver paint. In-plane temperature-dependent resistivity was recorded from room temperature (300 K) down to 10 K in a low pressure helium environment (~20 Torr).

Shown in Fig. 4a are temperature-dependent resistivity of pristine Mo_2CT_x and its heat-treated and gas treated derivatives. The room-temperature resistivity of pristine Mo_2CT_x, and Mo_2NT_x are 3.6×10^{-1} and 4.8×10^{-4} Ω cm, respectively. The resistivity of the pristine Mo_2CT_x is similar to that reported earlier.[45] Note that the pristine sample in this work refers to the as-synthesized film annealed in vacuum at 150 °C for 3 h to remove adsorbed and/or intercalated molecules. The resistivity of pristine Mo_2CT_x increases with decreasing temperature down to 40 K (a semiconductor-like behavior), after which the resistivity rises more sharply. This change in conduction mechanism in the low temperature regime was also observed in the previous report on Mo_2CT_x, which was attributed to the variable range hopping (VRH) mechanism.[45] In contrast, the resistivity of Mo_2NT_x first decreases when the temperature is decreased from 300 K to 100

K, and remains roughly constant down to 10 K. The drastic changes in both the absolute value of resistivity and the shape of resistivity versus temperature plot suggests changes in the conduction mechanism and/or electronic structure caused by ammoniation. Metallic conductivity observed for the Mo_2NT_x is consistent with that of bulk non-MXene Mo_2N.[62] For comparison, the precursor MXene Mo_2CT_x film was treated at 600 °C with the same conditions except that flowing Ar gas was used to create an inert environment instead of NH_3, to determine if the change in resistivity was dependent on heat-treatment regardless of the atmosphere, the atmosphere, or a combination of both. The resistivity of the Ar-treated Mo_2CT_x (Mo_2CT_x (Ar)) was measured to be 4.0×10^{-3} Ω cm and similar to Mo_2N, the Ar-treated Mo_2CT_x (Mo_2CT_x (Ar)) also shows decreasing resistivity with decreasing temperature. A clear metallic behavior of Mo_2CT_x (Ar) and Mo_2NT_x can be seen in Fig. S11. However, the room-temperature resistivity of Mo_2CT_x (Ar) is an order of magnitude higher than that of Mo_2NT_x. Hence, we conclude that the change in electronic conduction behavior of Mo_2CT_x MXene after ammoniation stems from synergistic effects of the transformation from carbide to nitride as well as the removal of intercalated molecules and surface functionalities at high temperature.

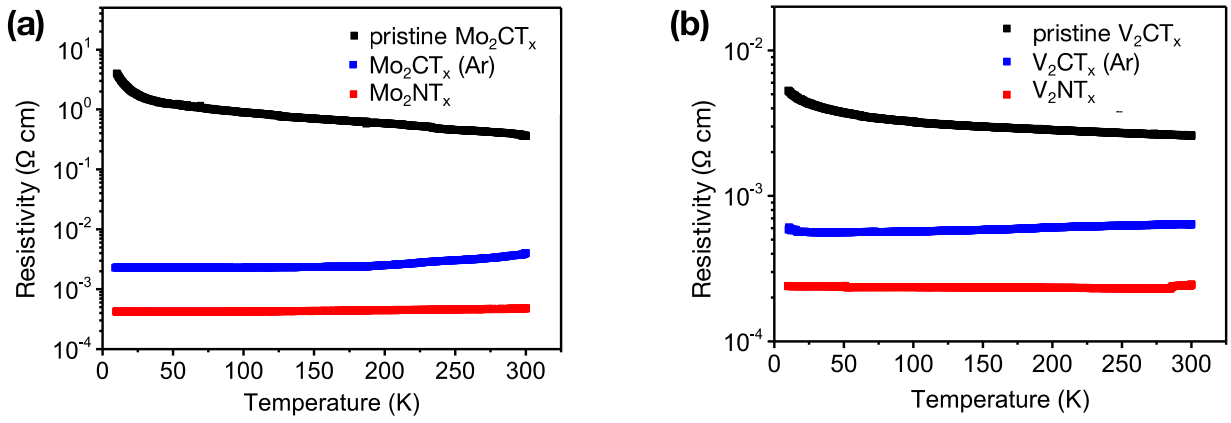

Fig. 4. Temperature-dependent resistivity of (a) Mo_2NT_x and (b) V_2NT_x. The various curves in each correspond to the pristine MXene precursor (Mo_2CT_x and V_2CT_x) (black curves), the MXene after treatment in Ar at 600 °C (Mo_2CT_x (Ar) and V_2CT_x (Ar)) (blue curves), and the

nitride Mo_2NT_x and V_2NT_x synthesized by treating their respective MXene precursors in NH_3 at 600 °C (red curves). The behavior of the dependence of resistivity on temperature changes as a result of the heat treatments to a more metallic behavior. The decrease in resistivity (increase in conductivity) is greatest after the pristine MXenes are treated in NH_3.

For V_2CT_x MXene, the room-temperature resistivity of pristine V_2CT_x, V_2CT_x (Ar), and V_2NT_x are 2.6×10^{-3}, 6.4×10^{-4}, and 2.4×10^{-4} Ω cm, respectively. Temperature-dependent resistivity of V_2CT_x MXene and its heat-treated derivative are presented in Fig. 4b. The pristine V_2CT_x shows semiconductor-like behavior where the resistivity increases from 2.6×10^{-3} Ω cm at room temperature to 5.3×10^{-3} Ω cm at 10 K. Similar to Mo_2CT_x, ammoniation and heat treatment of V_2CT_x in an inert environment lead to lower resistivity and change from semiconductor-like to metallic behavior. This change in behavior is consistent with first principle calculations that OH- and F-terminated V_2CT_x are small-bandgap semiconductor, while non-terminated monolayer V_2CT_x and V_2NT_x are metallic.[63, 64]

Conclusions

In summary, with different analytical techniques including SEM, EDX, XRD, and X-ray PDF we present evidence of the first transformation of MXene carbides (Mo_2CT_x and V_2CT_x) to 2D nitrides by ammoniation. This was achieved by ammoniating Mo_2CT_x and V_2CT_x MXenes at elevated temperatures (up to 600 ºC for 1 h). Nitridation lead to the replacement of C atoms with N atoms from the ammonia (NH_3) and transformed the carbide MXenes into nitrides. Based on our characterization results, ammoniation of Mo_2CT_x at 600 ºC for 1 h leads to a Mo_2NT_x with a layered MXene structure, where in contract to the MXene carbide, in-plane molybdenum bonds are shorter than their out of plane bonds. However, ammoniation of V_2CT_x at the same conditions yields a mixed phase of trigonal V_2N and cubic VN. Temperature-dependent resistivity determined that compared to pristine Mo_2CT_x and V_2CT_x, heat treating the samples at

600 ºC for 1 h in Ar and NH_3 increased the electrical conductivity by orders of magnitude, with ammoniation resulting in the greatest increase in electrical conductivity. These heat treatments also changed the temperature dependence of resistivity.

Conflicts of Interest

There are no conflicts of interest to declare.

Acknowledgements

We thank Christine Hatter for conducting preliminary TEM measurements, Patrick Walsh for help with MXene synthesis, as well as Saleesha Sin for designing the schematic of ammoniation (all Drexel University). This work was supported by the U.S. National Science Foundation under grant number DMR-1310245. This research used JEOL2100F HRTEM of the Center for Functional Nanomaterials, which is a U.S. DOE Office of Science Facility, at Brookhaven National Laboratory under Contract No. DE-SC0012704. X-ray PDF measurements were conducted on beamline 28-ID-2 of the National Synchrotron Light Source II, a U.S. Department of Energy (DOE) Office of Science User Facility operated for the DOE Office of Science by Brookhaven National Laboratory under Contract No. DE-SC0012704. Long Yang and Simon Billinge acknowledge financial support from the NSF MRSEC program through Columbia in the Center for Precision Assembly of Superstratic and Superatomic Solids (DMR-1420634). We also acknowledge support from the Drexel Areas of Research Excellence (DARE) initiative.

Notes and References

1. M. Naguib, M. Kurtoglu, V. Presser, J. Lu, J. Niu, M. Heon, L. Hultman, Y. Gogotsi and M. W. Barsoum, *Advanced Materials*, 2011, **23**, 4248-4253.

2. B. Anasori, M. R. Lukatskaya and Y. Gogotsi, *Nature Reviews Materials*, 2017, **2**, 16098.
3. P. Eklund, J. Rosen and P. O. Å. Persson, *Journal of Physics D: Applied Physics*, 2017, **50**, 113001.
4. M. Khazaei, A. Ranjbar, M. Arai, T. Sasaki and S. Yunoki, *Journal of Materials Chemistry C*, 2017, **5**, 2488-2503.
5. V. M. H. Ng, H. Huang, K. Zhou, P. S. Lee, W. Que, J. Z. Xu and L. B. Kong, *Journal of Materials Chemistry A*, 2017, **5**, 3039-3068.
6. M. Ghidiu, M. R. Lukatskaya, M.-Q. Zhao, Y. Gogotsi and M. W. Barsoum, *Nature*, 2014, **516**, 78-81.
7. M. R. Lukatskaya, O. Mashtalir, C. E. Ren, Y. Dall'Agnese, P. Rozier, P. L. Taberna, M. Naguib, P. Simon, M. W. Barsoum and Y. Gogotsi, *Science*, 2013, **341**, 1502-1505.
8. M. Naguib, J. Halim, J. Lu, K. M. Cook, L. Hultman, Y. Gogotsi and M. W. Barsoum, *J Am Chem Soc*, 2013, **135**, 15966-15969.
9. M.-Q. Zhao, C. E. Ren, Z. Ling, M. R. Lukatskaya, C. Zhang, K. L. Van Aken, M. W. Barsoum and Y. Gogotsi, *Advanced Materials*, 2015, **27**, 339-345.
10. F. Shahzad, M. Alhabeb, C. B. Hatter, B. Anasori, S. Man Hong, C. M. Koo and Y. Gogotsi, *Science*, 2016, **353**, 1137-1140.
11. J. Liu, H.-B. Zhang, R. Sun, Y. Liu, Z. Liu, A. Zhou and Z.-Z. Yu, *Advanced Materials*, 2017, DOI: 10.1002/adma.201702367, 1702367.
12. K. Rasool, M. Helal, A. Ali, C. E. Ren, Y. Gogotsi and K. A. Mahmoud, *ACS Nano*, 2016, **10**, 3674-3684.
13. C. E. Ren, K. B. Hatzell, M. Alhabeb, Z. Ling, K. A. Mahmoud and Y. Gogotsi, *The Journal of Physical Chemistry Letters*, 2015, **6**, 4026-4031.
14. J. Halim, M. R. Lukatskaya, K. M. Cook, J. Lu, C. R. Smith, L.-Å. Näslund, S. J. May, L. Hultman, Y. Gogotsi, P. Eklund and M. W. Barsoum, *Chemistry of Materials*, 2014, **26**, 2374-2381.
15. A. D. Dillon, M. J. Ghidiu, A. L. Krick, J. Griggs, S. J. May, Y. Gogotsi, M. W. Barsoum and A. T. Fafarman, *Advanced Functional Materials*, 2016, **26**, 4162-4168.
16. K. Hantanasirisakul, M. Q. Zhao, P. Urbankowski, J. Halim, B. Anasori, S. Kota, C. E. Ren, M. W. Barsoum and Y. Gogotsi, *Advanced Electronic Materials*, 2016, **2**, 1600050.
17. B. Xu, M. Zhu, W. Zhang, X. Zhen, Z. Pei, Q. Xue, C. Zhi and P. Shi, *Advanced Materials*, 2016, **28**, 3333-3339.
18. C. J. Zhang, B. Anasori, A. Seral-Ascaso, S. H. Park, N. McEvoy, A. Shmeliov, G. S. Duesberg, J. N. Coleman, Y. Gogotsi and V. Nicolosi, *Advanced Materials*, 2017, DOI: 10.1002/adma.201702678.
19. M. Zhu, Y. Huang, Q. Deng, J. Zhou, Z. Pei, Q. Xue, Y. Huang, Z. Wang, H. Li, Q. Huang and C. Zhi, *Advanced Energy Materials*, 2016, **6**, 1600969.
20. H. Fashandi, M. Dahlqvist, J. Lu, J. Palisaitis, S. I. Simak, I. A. Abrikosov, J. Rosen, L. Hultman, M. Andersson, A. Lloyd Spetz and P. Eklund, *Nat Mater*, 2017, **16**, 814-818.
21. Q. Tao, M. Dahlqvist, J. Lu, S. Kota, R. Meshkian, J. Halim, J. Palisaitis, L. Hultman, M. W. Barsoum and P. O. Persson, *Nature Communications*, 2017, **8**.
22. G. V. Naik, J. L. Schroeder, X. Ni, A. V. Kildishev, T. D. Sands and A. Boltasseva, *Optical Materials Express*, 2012, **2**, 478-489.
23. B. Soundiraraju and B. K. George, *ACS Nano*, 2017, **11**, 8892-8900.

24. A. Morel, Y. Borjon-Piron, R. L. Porto, T. Brousse and D. Bélanger, *Journal of The Electrochemical Society*, 2016, **163**, A1077-A1082.
25. Y. Zhong, X. Xia, F. Shi, J. Zhan, J. Tu and H. J. Fan, *Advanced Science*, 2016, **3**, 1500286.
26. J. Xie, S. Li, X. Zhang, J. Zhang, R. Wang, H. Zhang, B. Pan and Y. Xie, *Chemical Science*, 2014, **5**, 4615-4620.
27. M. W. Barsoum, in *MAX Phases*, Wiley-VCH Verlag GmbH & Co. KGaA, 2013, DOI: 10.1002/9783527654581.ch1, pp. 1-12.
28. P. Urbankowski, B. Anasori, T. Makaryan, D. Er, S. Kota, P. L. Walsh, M. Zhao, V. B. Shenoy, M. W. Barsoum and Y. Gogotsi, *Nanoscale*, 2016, **8**, 11385-11391.
29. Q. Ye, P. Xiao, W. Liu, K. Chen, T. Chen, J. Xue, S. Du and Q. Huang, *RSC Advances*, 2015, **5**, 70339-70344.
30. Z. Y. Al Balushi, K. Wang, R. K. Ghosh, R. A. Vilá, S. M. Eichfeld, J. D. Caldwell, X. Qin, Y.-C. Lin, P. A. DeSario and G. Stone, *Nature materials*, 2016, **15**, 1166-1171.
31. I. R. Shein and A. L. Ivanovskii, *Computational Materials Science*, 2012, **65**, 104-114.
32. M. Sreedhara, K. Vasu and C. Rao, *Zeitschrift für anorganische und allgemeine Chemie*, 2014, **640**, 2737-2741.
33. S. Sakthivel and H. Kisch, *ChemPhysChem*, 2003, **4**, 487-490.
34. G. Liu, L. Wang, C. Sun, X. Yan, X. Wang, Z. Chen, S. C. Smith, H.-M. Cheng and G. Q. Lu, *Chemistry of Materials*, 2009, **21**, 1266-1274.
35. Y. Wen, T. E. Rufford, X. Chen, N. Li, M. Lyu, L. Dai and L. Wang, *Nano Energy*, 2017, **38**, 368-376.
36. X. Xiao, H. Yu, H. Jin, M. Wu, Y. Fang, J. Sun, Z. Hu, T. Li, J. Wu, L. Huang, Y. Gogotsi and J. Zhou, *ACS Nano*, 2017, **11**, 2180-2186.
37. X. Xiao, H. Song, S. Lin, Y. Zhou, X. Zhan, Z. Hu, Q. Zhang, J. Sun, B. Yang, T. Li, L. Jiao, J. Zhou, J. Tang and Y. Gogotsi, *Nat. Commun.*, 2016, **7**, 11296.
38. M. Khazaei, M. Arai, T. Sasaki, M. Estili and Y. Sakka, *Physical Chemistry Chemical Physics*, 2014, **16**, 7841-7849.
39. R. Meshkian, L.-Å. Näslund, J. Halim, J. Lu, M. W. Barsoum and J. Rosen, *Scripta Materialia*, 2015, **108**, 147-150.
40. C. Xu, L. Wang, Z. Liu, L. Chen, J. Guo, N. Kang, X.-L. Ma, H.-M. Cheng and W. Ren, *Nature materials*, 2015, **14**, 1135-1141.
41. D. Geng, X. Zhao, Z. Chen, W. Sun, W. Fu, J. Chen, W. Liu, W. Zhou and K. P. Loh, *Advanced Materials*, 2017, DOI: 10.1002/adma.201700072.
42. H. Kim, B. Anasori, Y. Gogotsi and H. N. Alshareef, *Chemistry of Materials*, 2017, **29**, 6472-6479.
43. J. Zhou, X. Zha, X. Zhou, F. Chen, G. Gao, S. Wang, C. Shen, T. Chen, C. Zhi, P. Eklund, S. Du, J. Xue, W. Shi, Z. Chai and Q. Huang, *ACS Nano*, 2017, **11**, 3841-3850.
44. J. Zhou, X. Zha, F. Y. Chen, Q. Ye, P. Eklund, S. Du and Q. Huang, *Angewandte Chemie*, 2016, **128**, 5092-5097.
45. J. Halim, S. Kota, M. R. Lukatskaya, M. Naguib, M. Q. Zhao, E. J. Moon, J. Pitock, J. Nanda, S. J. May and Y. Gogotsi, *Advanced Functional Materials*, 2016, **26**, 3118-3127.
46. J. Landoulsi, M. J. Genet, S. Fleith, Y. Toure, I. Liascukiene, C. Methivier and P. G. Rouxhet, *Applied Surface Science*, 2016, **383**, 71-83.

47. K. D. Fredrickson, B. Anasori, Z. W. Seh, Y. Gogotsi and A. Vojvodic, *The Journal of Physical Chemistry C*, 2016, **120**, 28432-28440.
48. T. Huang, S. Mao, G. Zhou, Z. Wen, X. Huang, S. Ci and J. Chen, *Nanoscale*, 2014, **6**, 9608-9613.
49. X. Zhou, H. Chen, D. Shu, C. He and J. Nan, *Journal of Physics and Chemistry of Solids*, 2009, **70**, 495-500.
50. T. Egami and S. J. Billinge, *Underneath the Bragg peaks: structural analysis of complex materials*, Newnes, 2 edn., 2012.
51. C. Shi, M. Beidaghi, M. Naguib, O. Mashtalir, Y. Gogotsi and S. J. Billinge, *Physical review letters*, 2014, **112**, 125501.
52. P. J. Chupas, X. Qiu, J. C. Hanson, P. L. Lee, C. P. Grey and S. J. Billinge, *Journal of Applied Crystallography*, 2003, **36**, 1342-1347.
53. P. Juhás, T. Davis, C. L. Farrow and S. J. Billinge, *Journal of applied Crystallography*, 2013, **46**, 560-566.
54. X. Yang, P. Juhas, C. L. Farrow and S. J. Billinge, *arXiv preprint arXiv:1402.3163*, 2014.
55. T. Proffen and S. Billinge, *Journal of Applied Crystallography*, 1999, **32**, 572-575.
56. C. Farrow, P. Juhas, J. Liu, D. Bryndin, E. Božin, J. Bloch, T. Proffen and S. Billinge, *Journal of Physics: Condensed Matter*, 2007, **19**, 335219.
57. P. Juhás, C. L. Farrow, X. Yang, K. R. Knox and S. J. Billinge, *Acta Crystallographica. A*, 2015, **71**, 562-568.
58. A. N. Christensen and B. Lebech, *Acta Crystallographica Section B: Structural Crystallography and Crystal Chemistry*, 1979, **35**, 2677-2678.
59. S. Hosoya, T. Yamagishi and M. Tokonami, *Journal of the Physical Society of Japan*, 1968, **24**, 363-367.
60. K. Fukuda, M. Morita, S. Toyoda, A. Nakata, K. Tanaka, Y. Uchimoto and E. Matsubara, *Chemistry of Materials*, 2016, **28**, 8899-8904.
61. P. Debye, *Annalen der Physik*, 1915, **351**, 809-823.
62. V. Anitha, S. Major, D. Chandrashekharam and M. Bhatnagar, *Surface and Coatings Technology*, 1996, **79**, 50-54.
63. J. Hu, B. Xu, C. Ouyang, S. A. Yang and Y. Yao, *The Journal of Physical Chemistry C*, 2014, **118**, 24274-24281.
64. G. Gao, G. Ding, J. Li, K. Yao, M. Wu and M. Qian, *Nanoscale*, 2016, **8**, 8986-8994.

2D molybdenum and vanadium nitrides synthesized by ammoniation of 2D transition metal carbides (MXenes)

Patrick Urbankowski,[1] Babak Anasori,[1] Kanit Hantanasirisakul,[1] Long Yang,[2] Lihua Zhang,[3] Bernard Haines,[1] Steven J. May,[1] Simon J. L. Billinge,[2,4] Yury Gogotsi[1†]

[1]A.J. Drexel Nanomaterials Institute and Department of Materials Science & Engineering, Drexel University, Philadelphia, PA 19104, USA
[2]Department of Applied Physics and Applied Mathematics, Columbia University, New York, NY 10027, USA
[3]Center for Functional Nanomaterials, Brookhaven National Laboratory, Upton, NY 11973, USA
[4]Condensed Matter Physics and Materials Science Department, Brookhaven National Laboratory, Upton, NY 11973, USA

[†]Corresponding author:
Y. Gogotsi (gogotsi@drexel.edu) Tel.: +1-215-895-6446 Fax: +1-215-895-1934

1 Synthesis of Mo_2Ga_2C and Mo_2CT_x

Synthesis of Mo_2Ga_2C: Mo_2CT_x was synthesized by etching a Mo_2Ga_2C powder precursor. Mo_2Ga_2C powder was synthesized by a solid-liquid reaction in which -325 mesh Mo_2C powder and Ga (both Alfa Aesar, Ward Hill, MA, 99.5 wt% purity) were mixed in a 1 : 8 molar ratio.[1] This mixture was placed in a quartz tube that was evacuated of air using a vacuum pump and then sealed.[1] The tube was then placed in a tube furnace that was heated to 850 °C at a rate of 10 °C min^{-1}, and then held at that temperature for 48 h.[1] After the furnace cooled, the material was crushed using a mortar and pestle, and then returned to the quartz tube.[1] The tube was then evacuated and reheated to 850 °C at a rate of 10 °C min^{-1} and then held for 16 h.[1] 1 g of Mo_2Ga_2C powder was washed in a 20 mL solution of 12 M hydrochloric acid (HCl) (technical grade, Fisher Scientific, Fair Lawn, NJ) for 48 h at room temperature (RT) while being stirred with a Teflon coated magnet on a stirring plate to remove any unreacted Ga.[1] The powders were washed with deionized (DI) water several times until a pH of 6 was reached, then filtered to dry the powder using a nanoporous polypropylene membrane (3501 Coated PP, 0.064 µm pore size, Celgard, USA).

Synthesis of delaminated Mo_2CT_x: 2 g of Mo_2Ga_2C powder was added to a bottle with 20 mL of 14 M HF solution (Fisher Scientific, Fair Lawn, NJ). Afterwards, the bottle was placed in an oil bath over a stirring hot plate and held at 55 °C for 72 h with stirring using a Teflon coated magnet in the bottle. The resulting suspension was washed with DI water several times until a pH of at least 6 was reached. Each time water was added to the centrifuge tube containing the product and water; it was then shaken before centrifuging at 3500 rpm for 2 min. The powder was then filtered and dried over a nanoporous polypropylene membrane (3501 Coated PP, 0.064 µm pore size, Celgard, USA). This product is referred to as multilayered Mo_2CT_x. 1 g of the powder was mixed with 10 mL of an aqueous solution of 54-56 wt.% tetrabutylammonium hydroxide (TBAOH) (Sigma Aldrich, St. Louis, MO, USA). The mixture was stirred for 1 h at RT. The mixture was then washed with 40 mL of DI water and centrifuged at 3500 rpm for 5 min. The mixture was washed three times. After washing, the powder sediment was bath

sonicated in a bottle of 50 mL of deionized water for 1 h. The suspension was then centrifuged at 3500 rpm for 1 h. The supernatant suspension was then filtered over nanoporous polypropylene membrane (3501 Coated PP, 0.064 µm pore size, Celgard, USA). This yielded a film of delaminated Mo_2CT_x (d-Mo_2CT_x).

2 Synthesis of V_2C and V_2CT_x

Synthesis of V_2AlC: V_2CT_x was synthesized by etching a V_2AlC powder precursor. V_2AlC powders were synthesized mixing -325 mesh vanadium, V and Al powders (both Alfa Aesar, Ward Hill, MA, 99.5 wt.% purity) and graphite, C (Alfa Aesar Ward Hill, USA, 99 wt.% purity; -300 mesh) were mixed in a 2.0 : 1.1 : 1.0 molar ratio.[2] The mixture was mixed and then placed in an alumina crucible boat which was placed in a tube furnace. The mixture was heated to 1600 °C at a rate of 5 °C/min under flow of argon, Ar, and held at that temperature for 4 h before cooling to RT. The resulting sintered blocks were milled using a titanium-nitride-coated milling bit to form powder. The powder was then sieved so that -400 mesh size particles were used for further treatment.

Synthesis of delaminated V_2CT_x: 2 g of V_2AlC powder was added to a bottle with 20 mL of 14 M HF solution (Fisher Scientific, Fair Lawn, NJ). Afterwards, the bottle was placed in an oil bath over a stirring hot plate and held at 35 °C for 24 h with stirring using a Teflon coated magnet in the bottle. The resulting suspension was washed with DI water several times until a pH of at least 6 was reached. Each time water was added to the centrifuge tube containing the product and water, it was then shaken before centrifuging at 3500 rpm for 2 min. The powder was then filtered and dried over a nanoporous polypropylene membrane (3501 Coated PP, 0.064 µm pore size, Celgard, USA). This product is referred to as multilayered V_2CT_x. 1 g of the resulting powder was mixed with 10 mL of an aqueous solution of 54-56 wt.% tetrabutylammonium hydroxide (TBAOH) (Sigma Aldrich, St. Louis, MO, USA). The mixture was stirred for 1 h at RT. The mixture was then washed with 40 mL of DI water and centrifuged at 3500 rpm for 5 min. The mixture was washed three times. After washing, the powder sediment was bath sonicated in a bottle of 50 mL of deionized water for 1 h. The suspension was then centrifuged at 3500 rpm for 1 h. The supernatant suspension was then filtered over nanoporous polypropylene membrane (3501 Coated PP, 0.064 µm pore size, Celgard, USA). This yielded a film of delaminated V_2CT_x (d-V_2CT_x).

Ammoniation of delaminated MXene films: Ammonia, NH_3, gas (anhydrous grade 4, Airgas, Philadelphia, PA, USA) flowing through a quartz tube in a Carbolite (Hope Valley, UK) tube furnace at a flowrate of 300 cm^3/min was used to nitridize the MXene films. The samples were heated to 400 °C, 500 °C or 600 °C at a rate of 5 °C/min and dwelled at the target temperature for 1 h.

3 Scanning Electron Microscopy

To examine the morphology and composition of the nitrides, scanning electron microscopy (SEM) was performed in a Zeiss Supra 50VP (Carl Zeiss SMT AG, Oberkochen, Germany) equipped with an energy-dispersive X-ray spectrometer (EDX) (Oxford EDS, with INCA software). Most EDX scan were obtained at low magnification (100× to 200×) on at least 3 different 0.5 mm × 0.5 mm areas for 60 s on each location. Atomic ratios determined from atomic percentages were calculated by averaging the atomic percentages of all points scanned. To determine if oxides were formed after ammoniation at 600 °C, micrographs of the Mo_2N and

V_2N were taken, shown in Fig. S1. No separate cubic particles were found on the nitrides, confirming that no separate oxides were formed as a byproduct of this procedure or from oxidation of the nitride products.

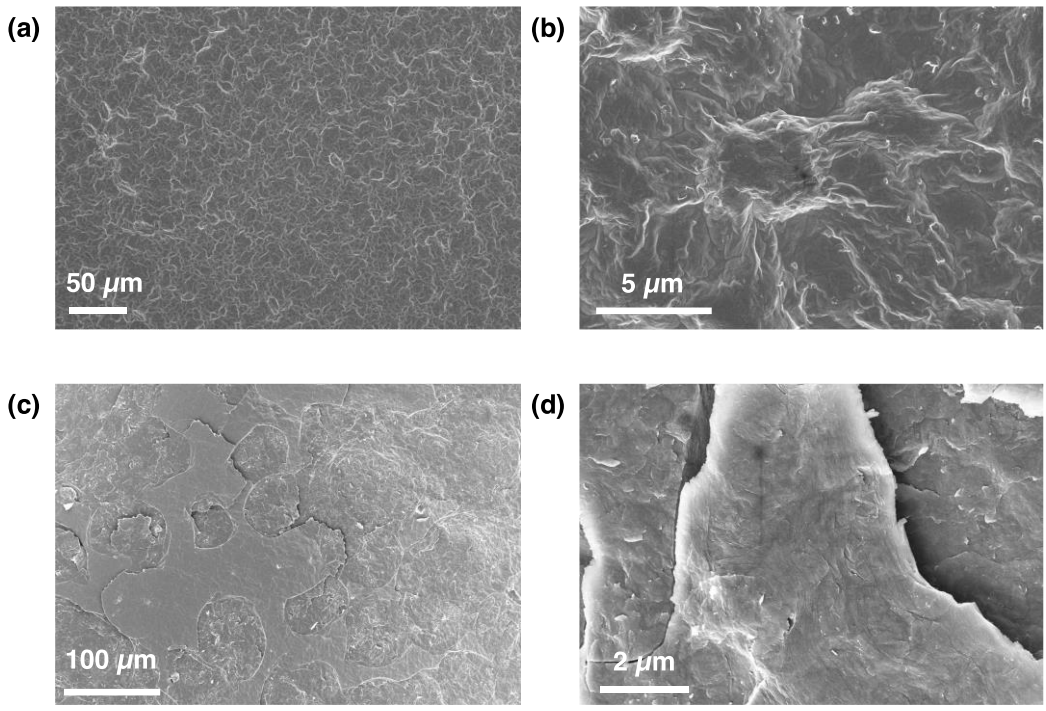

Fig. S1. Low and high magnification SEM images of Mo_2N and V_2N produced after annealing Mo_2CT_x and V_2CT_x films, respectively, in ammonia at 600 °C for 1 h. The absence of any cubic particles confirms that no oxides are formed from oxidation of the precursor MXene. (a) Low magnification of Mo_2N. (b) High magnification image of Mo_2N in (a). (c) Low magnification of V_2N. (d) High magnification image of V_2N in (c).

4 X-ray Photoelectron Spectroscopy

X-ray photoelectron spectroscopy (XPS) spectra of the Mo_2NT_x and V_2NT_x films were measured by a spectrometer (Physical Electronics, VersaProbe 5000, Chanhassen, MN) employing a 100 μm monochromatic Al Kα X-ray beam to irradiate each sample's surface. Photoelectrons were collected by a takeoff angle of 180° between the sample surface of each sample and the path to the analyzer. Charge neutralization was applied using a dual beam charge neutralizer irradiating low-energy electrons and ion beam to avoid shift in the recorded BE. High-resolution spectra for Mo 3d, C 1s, Mo $3p_{3/2}$, N 1s, V 2p and O 1s were taken at a pass energy of 11.75 eV with a step size of 0.05 eV. The binding energy scale of all XPS spectra was references to the Fermi-edge (E_F), which was set to a BE of zero eV for each sample. The films were mounted on double-sided tape and were electrically grounded using a copper wire. Quantification and deconvolution of the core-level spectra was performed using a software package (CasaXPS Version 2.3.16 RP 1.6). Background contributions to the measured intensities were subtracted using a Shirley function prior to quantification and deconvolution. For the Mo_2NT_x film's spectra, intensity ratios of the $3d_{5/2}$ and $3d_{3/2}$ peaks were constrained to be 3:2. For the V_2NT_x film's spectra,

intensity ratios of the $2p_{3/2}$ and $2p_{1/2}$ peaks were constrained to be 2:1. The components of all regions scanned for for Mo_2NT_x are listed in Table S1. For Mo_2N, the high-resolution spectrum of the Mo 3d region (Figure S2a) were fitted by components corresponding to the two species N–Mo–T_x and MoO_3. It is important to note that, for both the Mo_2N and V_2N, no F in XPS after the ammoniation of their MXene precursor, where F functional groups are typically detected.[3] The components of all regions scanned for for V_2NT_x are listed in Table S2. For V_2NT_x, the high-resolution spectrum of the V 2p region (Figure S2d) were fitted by components corresponding to the following four species: metallic V, V^{3+}, V^{4+} and V^{5+}.

Table S1. Summary of global atomic compositions of the high resolution XPS region fittings of multilayered Mo_2NT_x, shown in Fig. 1c and Fig. S2a-c.

Region	BE [eV]	FWHM [eV]	Fraction	Assigned to	Reference
Mo $3d_{5/2}$ ($3d_{3/2}$)	229.0 (232.2)	1.0 (1.1)	0.21	N–Mo–T_x	[4]
	231.6 (235.3)	0.6 (1.1)	0.01	MoO_3	[1]
C 1s	283.1	0.9	0.01	C–Mo–T_x	[4]
	285.0	1.5	0.18	C–C	[1]
	286.6	1.4	0.03	CH_x/C–O	[1]
	288.7	2.0	0.02	COO	[1]
N 1s / Mo $3p_{3/2}$	395.1	2.5	0.21	Mo–N (Mo $3p_{3/2}$)	[4]
	397.5	1.5	0.22	Mo–N (N 1s)	[4]
	399.2	2.0	0.02	MoO_3 (Mo $3p_{3/2}$)	[1]
O 1s	530.9	1.4	0.03	N–Mo–O_x	[1]
	532.1	1.4	0.03	N–Mo–$(OH)_x$	[1]
	530.1	1.2	0.02	MoO_3	[1]
	533.6	1.5	0.01	N–Mo–OH–H_2O	[1]
Total			1.00		

Table S2. Summary of global atomic compositions of the high resolution XPS region fittings of multilayered V_2NT_x, shown in Fig. 1d and Fig. S2d-f.

Region	BE [eV]	FWHM [eV]	Fraction	Assigned to	Reference
C 1s	284.8	1.6	0.18	C–C	[5]
	286.3	1.4	0.04	CH_x/C–O	[5]
	288.0	2.0	0.03	C–N	[5]
N 1s	396.9	1.2	0.18	V–N	[6]
	398.3	3.2	0.11	N–C	[7]
V $2p_{3/2}$ ($2p_{1/2}$)	513.2 (520.2)	0.6 (1.2)	0.02	V^{0+}	[8]
	514.1 (521.3)	1.8 (2.2)	0.21	V^{3+} (V–N)	[9]
	516.0 (523.0)	1.5 (1.5)	0.09	V^{4+}	[8]
	517.1 (524.6)	1.5 (1.8)	0.04	V^{5+}	[8]
O 1s	530.1	1.7	0.07	V–O	[8]
	532.0	2.0	0.03	N–O	[10]
Total			1.00		

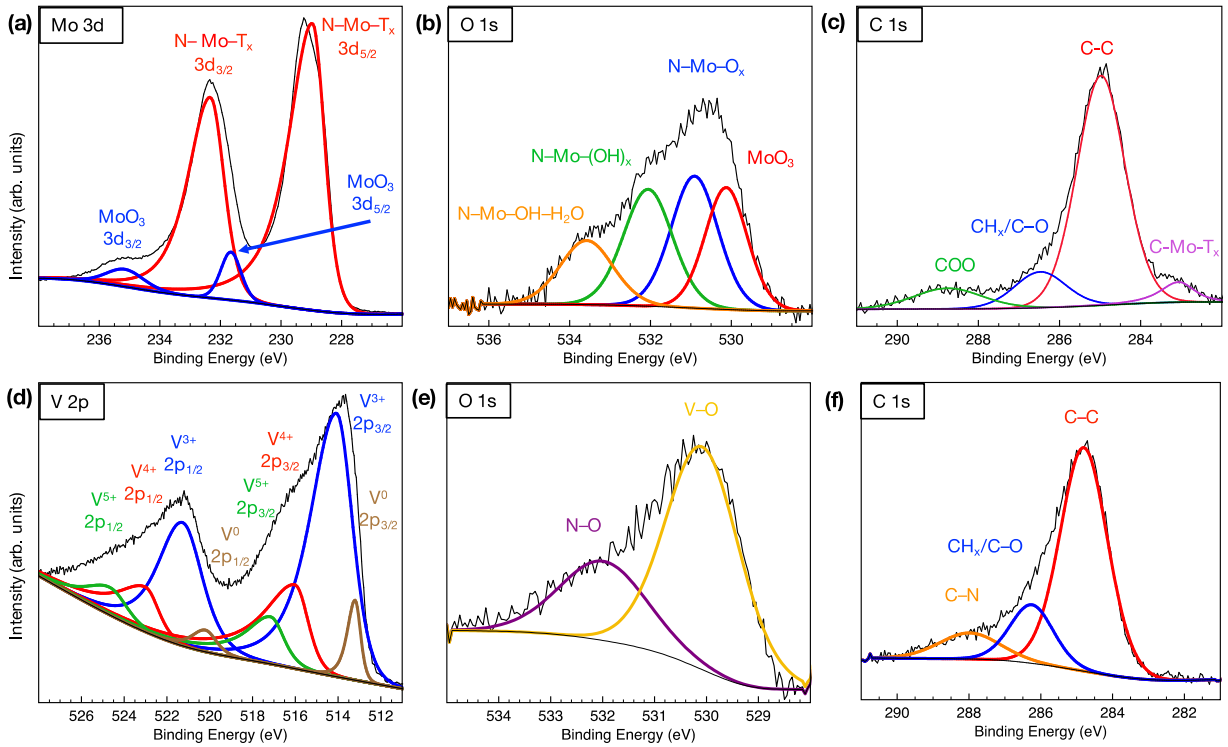

Figure S2. (a-c) High resolution XPS spectra for Mo_2NT_x synthesized by annealing delaminated Mo_2CT_x at 600 °C for 1 h in NH_3 (ammonia). Regions for Mo_2NT_x shown are (a) Mo 3d, (b) O 1s and (c) C 1s, showing evidence of Mo–N bonding in (a). (d-f) High resolution XPS spectra for V_2NT_x synthesized by annealing delaminated V_2CT_x at 600 °C for 1 h in ammonia. Regions scanned for V_2NT_x shown are (d) V 2p, (e) O 1s and (f) C 1s.

5 X-ray Diffraction

X-ray diffraction (XRD) was carried out on the Mo_2CT_x, V_2CT_x, Mo_2NT_x and V_2NT_x films using a Rigaku Smartlab (Tokyo, Japan) diffractometer with Cu-Kα radiation (40 kV and 44 mA); step size 0.02°, 3-50° 2θ range, step time of 1 s, 5 × 10 mm^2 window slit. To investigate the change in crystal structure as temperature of ammoniation increases, XRD was performed after ammoniation of the Mo_2CT_x and V_2CT_x at 400 °C or 500 °C for 1 h, shown in Fig. S3. For Mo_2NT_x, the basal plane (002) MXene peak increases from 2θ = 7° to 9°, indicating that the layered sheets are being annealed and more closely spaced. A peak at 25°, the source of which is uncertain, becomes more prominent but vanishes if the Mo_2CT_x is annealed at 600 °C instead of the temperatures below 600 °C. For the V_2NT_x patterns, the broad peak at 2θ = 25° can be attributed to the glass slide on which the films were scanned.[11] A peak at 37 °C becomes more and more prominent as ammoniation temperature increases, which may possibly be a competing non-MXene nitride phase.

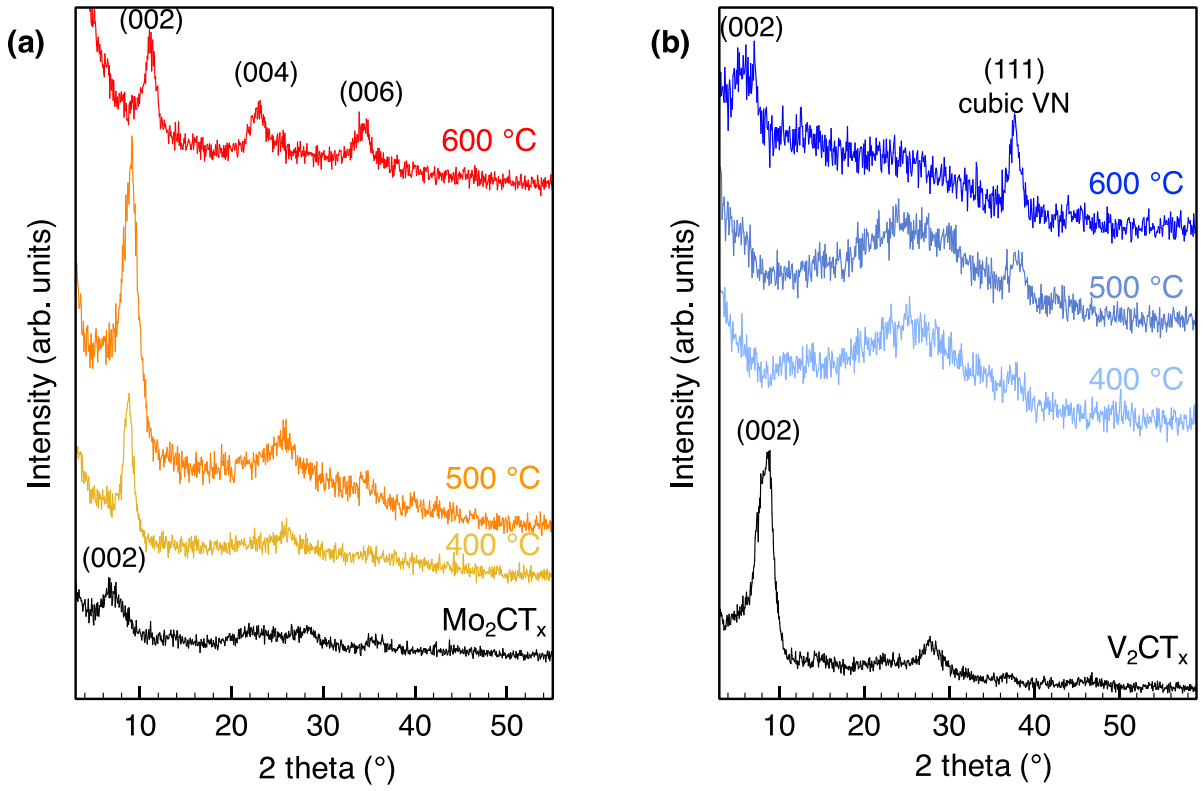

Figure S3. XRD patterns of (a) Mo_2CT_x and (b) V_2CT_x before and after (Mo_2NT_x and V_2NT_x) annealing in ammonia gas at various temperatures for 1 h. (a) For Mo_2NT_x, as the temperature of ammoniation increases, the (002) peak shifts from ~7° to ~11° at 600 °C. At ammoniation temperatures below 600 °C, a peak at about 25° becomes more prominent, but vanishes when nitridation temperature increases to 600 °C. (b) For V_2NT_x, as temperature of ammoniation increases, the peak at 37°, corresponding to a cubic VN, becomes more prominent.

6 X-ray Pair Distribution Function (PDF) Analysis

Synchrotron X-ray total scattering experiments were carried out at the X-ray Powder Diffraction (XPD) beamline, 28-ID-2, at the National Synchrotron Light Source II (NSLS II) at Brookhaven National Laboratory (BNL). The samples were crushed into powders, packed into 1 mm inner diameter kapton capillary tubes and measured at 100 K using a flowing nitrogen cryocooler. The rapid acquisition PDF technique (RaPDF)[12] was used with an X-ray energy of 67.14 keV (λ = 0.1847 Å). A large area 2D Perkin Elmer detector (2048 × 2048 pixels and 200 × 200 µm pixel size) was mounted orthogonal to the beam path with sample-to-detector distance of 205.39 mm behind the samples. The raw 2D data were azimuthally integrated and converted to 1D intensity versus the magnitude of the scattering momentum transfer Q using FIT2D.[13] $Q = 4\pi \sin\theta/\lambda$ for a scattering angle of 2θ and an X-ray wavelength of λ. The software xPDFsuite[14, 15] was used to correct and normalize the diffraction data and then Fourier transform them to obtain the experimental PDF, $G(r)$, according to:

$$G(r) = \frac{2}{\pi}\int_{Q_{min}}^{Q_{max}} Q[S(Q) - 1]\sin(Qr)\, dQ$$

where the total scattering structure function $S(Q)$ is the properly corrected and normalized powder diffraction intensity measured from Q_{min} to Q_{max}, governed by the experimental setup.[16] $G(r)$ gives the probability of finding a pair of atoms separated by a distance of r. Nickel was measured as the standard material to calibrate the sample-to-detector distance and to determine the Q_{damp} and Q_{broad} which are parameters that correct the PDF envelope function for the instrument resolution effects.[17, 18] The refined values Q_{damp} = 0.0369 Å^{-1} and Q_{broad} = 0.0131 Å^{-1} were fixed in the subsequent structure refinements of the PDF data. Structural modeling and refinement of PDF data was carried out using the PDFgui[18] and DiffPy-CMI programs.[19] Least-squares fits were performed by minimizing the fit residual, with the goodness-of-fit R_ω, given by:

$$R_\omega = \sqrt{\frac{\sum_{i=1}^{n}[G_{obs}(r_i) - G_{calc}(r_i,\ P)]^2}{\sum_{i=1}^{n} G_{obs}(r_i)^2}}$$

where G_{obs} and G_{calc} are the experimental and calculated PDFs and P is the set of parameters refined in the model.

6.1 Structure Refinement of V_2N

The initial structural model for the V_2N was a trigonal *P*-31*m* structure and the atoms are on the following special positions: V (x, 0, z), N1 (1/3, 2/3, 1/2), and N2 (0, 0, 0) shown in Fig. S4.[20] The structure refinements were performed over full-*r* (1.5 to 60 Å), low-*r* (1.5 to 20 Å), and high-*r* (20 to 60 Å) ranges separately, as shown in Fig. S5.

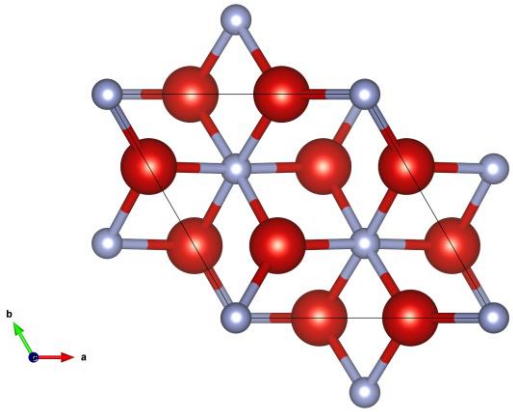

Figure S4. Trigonal V_2N (space group *P*-31*m*) structure projected along the [001] direction. Red atoms indicate V, blue atoms indicate N.

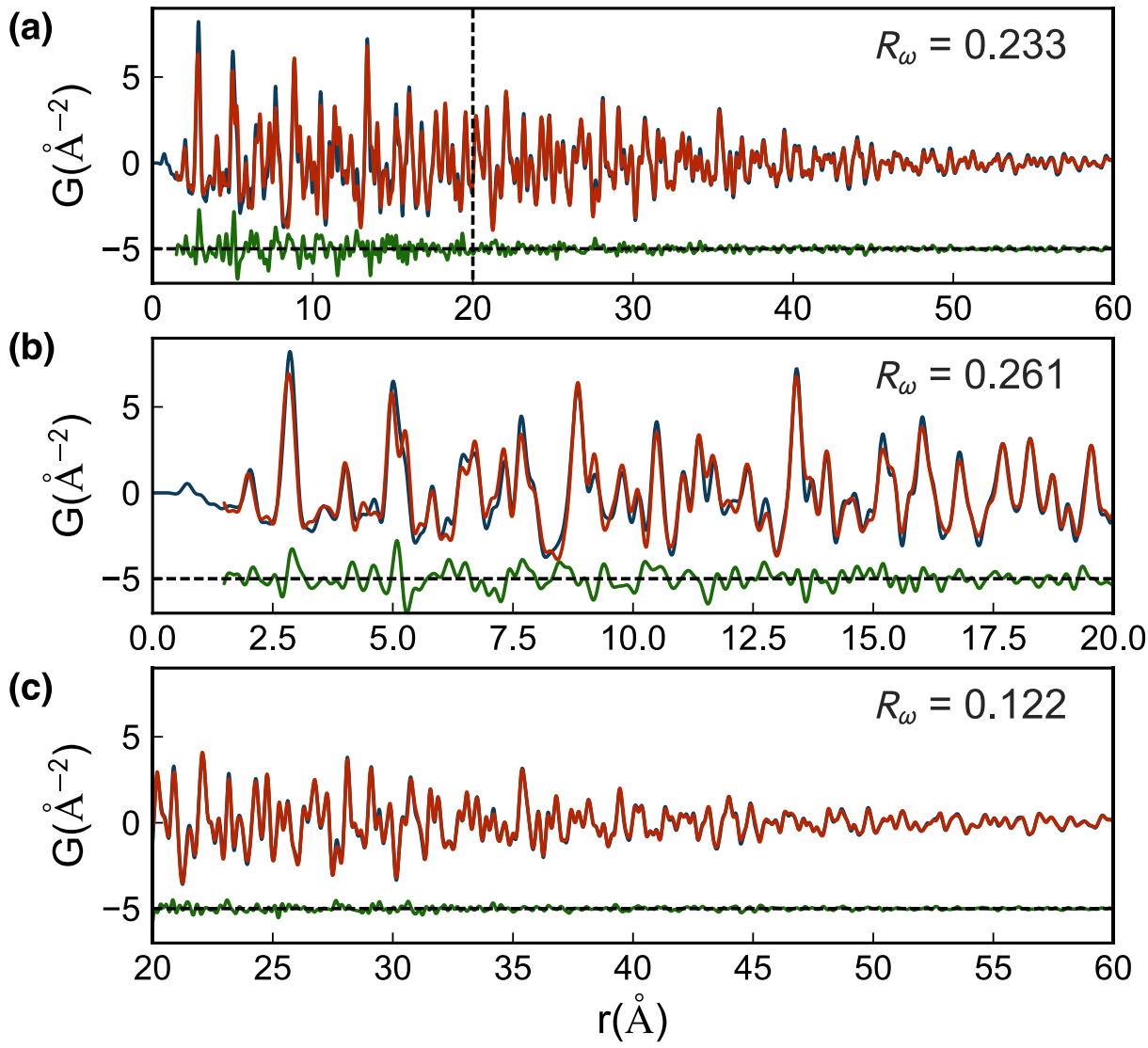

Figure S5. PDF fits (red curve) of the V_2N structure model to the measured data (blue) with difference curve offset below (green) over (a) full-*r* (1.5 to 60 Å), (b) low-*r* (1.5 to 20 Å), and (c) high-*r* (20 to 60 Å) ranges.

Table S3. Structure refinement results of V_2N structure model in the *r*-range of 1.5 to 60 Å, 1.5 to 20 Å, and 20 to 60 Å.

Fitting Range (Å)	1.5 to 60	1.5 to 20	20 to 60
R_ω	0.233	0.261	0.122
a (Å)	5.0421	5.0415	5.0423
c (Å)	4.3712	4.3717	4.3714
x (V)	0.6670	0.6671	0.6705
z (V)	0.7452	0.7449	0.7500
U_{iso}(V) (Å ^{2})	0.0037	0.0033	0.0034
U_{iso}(N) (Å ^{2})	0.0326	0.0242	0.0144

R_ω of the high-*r* region (20 to 60 Å) fit, 0.122, is much lower than that of low-*r* region (1.5 to 20 Å), 0.261. This indicates that the V_2N (space group *P*-31*m*) structural model fits the long-range (20 to 60 Å) features well, but it does not describe the local structure completely. Because of this, a two-phase fit over the low-*r* range (1.5 to 20 Å) was then attempted.

To improve the local structure refinement, another phase, VN (space group is *Fm*-3*m*), shown in Fig. S6, was added as a second phase with a finite particle size. The atoms are on the following positions: V at (0, 0, 0) and N at (1/2, 1/2, 1/2).[21]

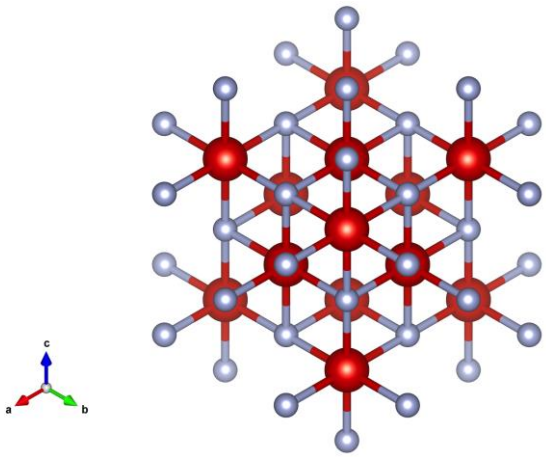

Figure S6. Cubic VN (space group *Fm*-3*m*) structure projected along the [111] direction. Red atoms indicate V, blue atoms indicate N.

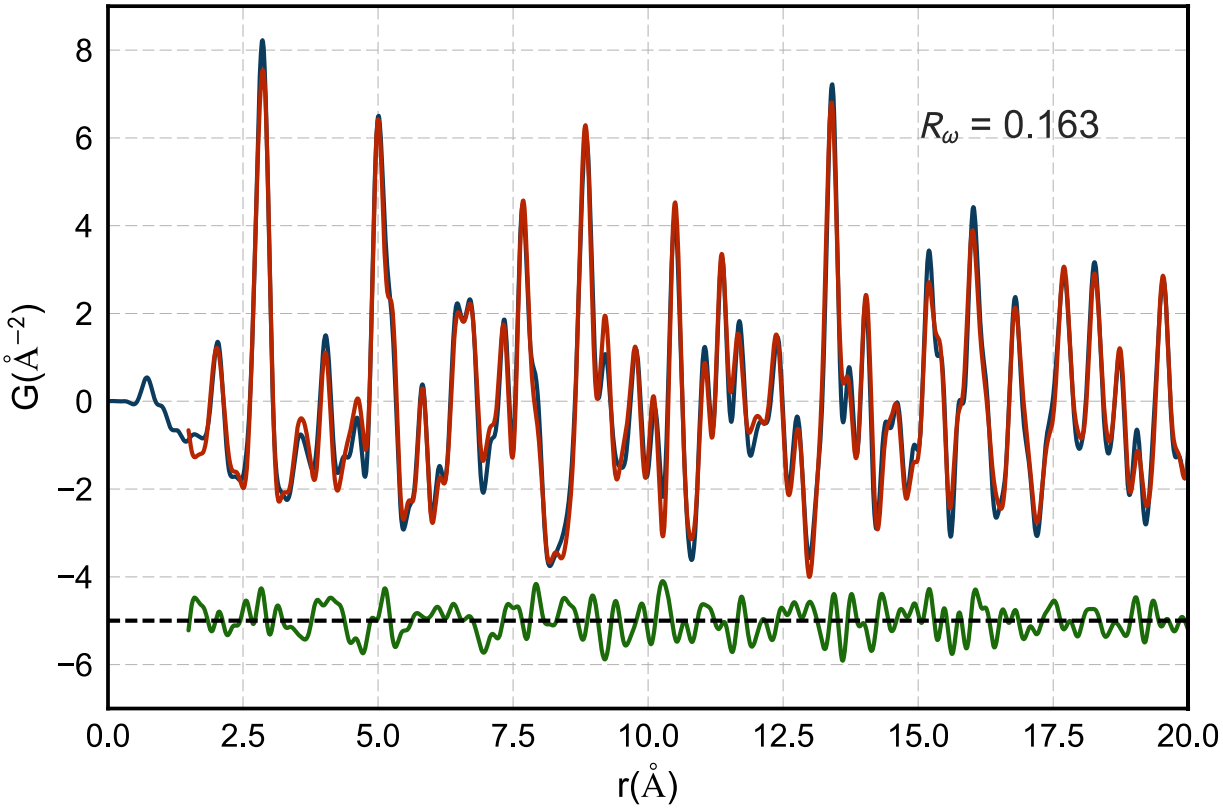

Figure S7. PDF fit (red curve) of the V_2N+VN mixed phase model to the measured data (blue) with difference curve offset below (green).

Table S4. Structure refinement result of V_2N + VN structure model in the *r*-range of 1.5 to 20 Å. For the VN phase, its lattice parameters were constrained as $a = c$ due to cubic symmetry, and its isotropic atomic displacement parameters U_{iso}(V) and U_{iso}(N) were constrained the same as those

in the V_2N phase. Spdiameter is the particle diameter parameter for PDF shape damping function.

Fitting Range (Å)	1.5 to 20 Å	
R_ω	0.163	
Phase	V_2N	VN
Mass Ratio	68%	32%
a (Å)	5.0382	4.1328
c (Å)	4.3748	4.1328
x (V)	0.6680	-
z (V)	0.7511	-
U_{iso} (V) ($Å^2$)	0.0033	0.0033
U_{iso} (N) ($Å^2$)	0.0110	0.0110
Spdiameter (Å)	-	22.3461

Comparing with the structure refinement result of V_2N in Table S2, the two-phase fit over the low-*r* range, 1.5 to 20 Å, (R_ω = 0.163) describes the local structure much better than the single-phase V_2N fit over the low-*r* range (R_ω = 0.261). The PDF fit of this mixed phase model over the full-*r* range (1.5 to 60 Å) is shown in Fig. 2b in the main text. The structure of Vanadium compound can be described as trigonal V_2N along with nanosized cubic VN.

6.2 Structure Refinement of Mo_2N

The Mo_2N single slab model (Fig. 2c in the main text) was initially built from the precursor Mo_2C MXene (*P*6$_3$/*mmc*) structure by replacing N atoms with C atoms at the same atomic positions, then cutting a single slab of atoms from its respective bulk crystal structure. The atoms are on the following special positions: Mo1 at (1/3, 2/3, *z*), Mo2 at (0, 0, *z*), and N (1/3, 2/3, *z*). We used the Debye scattering equation[22] to calculate the PDF of single slab using the DiffPy-CMI program.[19] The intralayer structure was refined to better fit the measured PDF of Mo_2N over the low-*r* range (1.5 to 5.5 Å). Starting from the carbide Mo_2C MXene precursor structure, the Mo_2N slab is squeezed along in-plane dimensions and extended along the out-of-plane dimension (z-direction) such that the distance between nearest Mo atoms on the same z-coordinate plane, for example Mo1-Mo2 in Fig. 2c, decreases from 3.3 Å to 2.9 Å, while the distance between nearest Mo atoms separated along the z-direction (but still within a single slab, e.g. Mo1-Mo3 in Fig. 2c) increases from 2.7 Å to 3.2 Å. The simulated PDF of the initial Mo_2N model before structure refinement, which has the same atomic positions as the precursor Mo_2C

model, is shown by the brown curve in Fig. 2d. It shows that ammoniation of Mo_2C changes the structure. The Mo_2N structure has the opposite of the distortion to the one in Mo_2C where the out-of-plane Mo-Mo distances are shorter than the in-plane Mo-Mo distances.

7 Transmission Electron Microscopy

Transmission Electron Microscopy (TEM) images were performed on JEOL2100F High Resolution TEM, at an accelerating voltage 200 kV. For TEM specimens, the multilayered MXenes (Mo_2CT_x and V_2CT_x) (not the delaminated MXenes as with all other measurements in this study) were ammoniated at 600 °C for 1 h. The nitride powders were subsequently stirred in an ethanol solution to form a diluted colloidal solution of nitride flakes. The TEM specimens were then prepared by dropping 3 drops of this colloidal solution onto a copper grid and drying in air.

8 Electrical Resistivity Measurements

Electronic properties of Mo_2CT_x and V_2CT_x before and after Ar and NH_3 heat treatment were studied in a Quantum Design EverCool II Physical Property Measurement System (PPMS). Free-standing films with a thickness of about 20 μm of each sample were cut to a 5 × 5 mm squares, and silver wires were attached onto each film in a 4-point probe geometry using adhesive silver paint. In-plane temperature-dependent resistivity was recorded from room temperature (300 K) down to 10 K in vacuum (~20 Torr) in a helium environment. The resistivity values were calculated according to:

$$\rho = \frac{\pi}{\ln 2} \; x \; R \; x \; t \; x \; FF$$

Where ρ = resistivity (Ω cm), R = resistance (Ω), t = film thickness (cm), FF = a correction factor based on the ratio of the probe distance to the film's dimension.

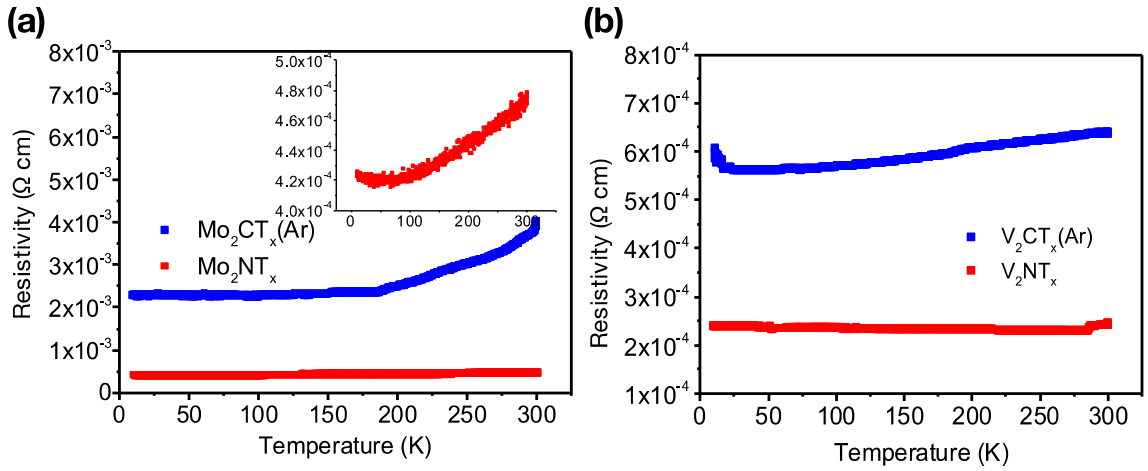

Figure S8. A zoom-in portion of the temperature-dependent resistivity of (a) Mo_2CT_x (Ar) and Mo_2NT_x and (b) V_2CT_x (Ar) and V_2NT_x.

References and Notes

1 J. Halim, S. Kota, M. R. Lukatskaya, M. Naguib, M. Q. Zhao, E. J. Moon, J. Pitock, J. Nanda, S. J. May and Y. Gogotsi, *Advanced Functional Materials*, 2016, **26**, 3118-3127.

2 M. Naguib, J. Halim, J. Lu, K. M. Cook, L. Hultman, Y. Gogotsi and M. W. Barsoum, *Journal of the American Chemical Society*, 2013, **135**, 15966-15969.

3 J. Halim, S. Kota, M. R. Lukatskaya, M. Naguib, M. Q. Zhao, E. J. Moon, J. Pitock, J. Nanda, S. J. May and Y. Gogotsi, *Advanced Functional Materials*, 2016.

4 R. Sanjinés, C. Wiemer, J. Almeida and F. Levy, *Thin Solid Films*, 1996, **290**, 334-338.

5 J. Halim, K. M. Cook, M. Naguib, P. Eklund, Y. Gogotsi, J. Rosen and M. W. Barsoum, *Applied Surface Science*, 2016, **362**, 406-417.

6 M. Romand and M. Roubin, *Analusis*, 1976, **4**, 308-312.

7 A. P. Dementjev, A. de Graaf, M. C. M. van de Sanden, K. I. Maslakov, A. V. Naumkin and A. A. Serov, *Diamond and Related Materials*, 2000, **9**, 1904-1907.

8 J. Kasperkiewicz, J. Kovacich and D. Lichtman, *Journal of electron spectroscopy and related phenomena*, 1983, **32**, 123-132.

9 A. Glaser, S. Surnev, F. Netzer, N. Fateh, G. Fontalvo and C. Mitterer, *Surface Science*, 2007, **601**, 1153-1159.

10 A. Pashutski and M. Folman, *Surface Science*, 1989, **216**, 395-408.

11 M. Stoica, G. N. B. M. de Macedo and C. Rüssel, *Optical Materials Express*, 2014, **4**, 1574-1585.

12 P. J. Chupas, X. Qiu, J. C. Hanson, P. L. Lee, C. P. Grey and S. J. Billinge, *Journal of Applied Crystallography*, 2003, **36**, 1342-1347.

13 A. Hammersley, S. Svensson, M. Hanfland, A. Fitch and D. Hausermann, *International Journal of High Pressure Research*, 1996, **14**, 235-248.

14 P. Juhás, T. Davis, C. L. Farrow and S. J. Billinge, *Journal of applied Crystallography*, 2013, **46**, 560-566.

15 X. Yang, P. Juhas, C. L. Farrow and S. J. Billinge, *arXiv preprint arXiv:1402.3163*, 2014.

16 T. Egami and S. J. Billinge, *Underneath the Bragg peaks: structural analysis of complex materials*, Newnes, 2 edn., 2012.

17 T. Proffen and S. Billinge, *Journal of Applied Crystallography*, 1999, **32**, 572-575.

18 C. Farrow, P. Juhas, J. Liu, D. Bryndin, E. Božin, J. Bloch, T. Proffen and S. Billinge, *Journal of Physics: Condensed Matter*, 2007, **19**, 335219.

19 P. Juhás, C. L. Farrow, X. Yang, K. R. Knox and S. J. Billinge, *Acta Crystallographica. A*, 2015, **71**, 562-568.

20 A. N. Christensen and B. Lebech, *Acta Crystallographica Section B: Structural Crystallography and Crystal Chemistry*, 1979, **35**, 2677-2678.

21 S. Hosoya, T. Yamagishi and M. Tokonami, *Journal of the Physical Society of Japan*, 1968, **24**, 363-367.

22 P. Debye, *Annalen der Physik*, 1915, **351**, 809-823.